

## Article

# Effect of $Y_2O_3$ Addition on Microstructure and Properties of Laser Cladded Al-Si Coatings on AZ91D Magnesium Alloy

Xiaofeng Wan <sup>1</sup>, Chuang Tian <sup>1</sup>, Yi Li <sup>1</sup>, Jingling Zhou <sup>1</sup>, Shuangqing Qian <sup>1</sup>, Lihong Su <sup>2,\*</sup> and Li Wang <sup>1,\*</sup> <sup>1</sup> School of Mechanical and Manufacturing Engineering, Nantong University, Nantong 226019, China<sup>2</sup> School of Mechanical, Materials, Mechatronic and Biomedical Engineering, University of Wollongong, Wollongong, NSW 2522, Australia

\* Correspondence: lihongsu@uow.edu.au (L.S.); wang1988@ntu.edu.cn (L.W.)

**Abstract:** The effect of  $Y_2O_3$  addition on the microstructure and properties of the laser cladded Al-Si alloy coating on the surface of AZ91D magnesium alloy was investigated in this study. The experimental results showed that the Al-Si +  $Y_2O_3$  cladding layers contained  $\alpha$ -Mg,  $Mg_2Si$ ,  $Al_4MgY$  and a small amount of  $Al_{12}Mg_{17}$  phases. The coarse dendrites, reticulated eutectic structures and massive phases in the coatings tended to be refined and gradually uniformly distributed with the increased amount of  $Y_2O_3$ . The introduction of  $Y_2O_3$  into the cladding layer favored the improvement of microhardness and wear resistance due to the grain refinement strengthening and dispersion strengthening. The addition of  $Y_2O_3$  also promoted the reduction of localized corrosion sites and made the corrosion surface smoother, implying that the corrosion resistance of the  $Y_2O_3$ -modified coatings was better than that of the unmodified cladding layer.

**Keywords:** AZ91D magnesium alloy; laser cladding; Al-Si +  $Y_2O_3$  coating; tribological property; wear resistance; corrosion resistance



**Citation:** Wan, X.; Tian, C.; Li, Y.; Zhou, J.; Qian, S.; Su, L.; Wang, L. Effect of  $Y_2O_3$  Addition on Microstructure and Properties of Laser Cladded Al-Si Coatings on AZ91D Magnesium Alloy. *Materials* **2023**, *16*, 338. <https://doi.org/10.3390/ma16010338>

Academic Editor: Antonio Riveiro

Received: 28 November 2022

Revised: 26 December 2022

Accepted: 28 December 2022

Published: 29 December 2022



**Copyright:** © 2022 by the authors. Licensee MDPI, Basel, Switzerland. This article is an open access article distributed under the terms and conditions of the Creative Commons Attribution (CC BY) license (<https://creativecommons.org/licenses/by/4.0/>).

## 1. Introduction

Magnesium alloy has the advantages of high specific strength and low density, and is currently a common light metal material [1–3]. In recent years, it has been widely used in the fields of automobile, aviation, national defense, medical and electronics [4–6]. Other benefits of magnesium alloys include their high machinability, good castability, hot formability, and recyclable nature [7–9]. However, the surface performance of magnesium alloys is typically poor due to high chemical reactivity, weak hardness, poor corrosion resistance, and poor wear characteristics, which restricts their wide range of applications in various industries [10–13]. According to Abbas et al. [10], the wear rate of as-received magnesium alloy was greatly higher than the samples subjected to a laser remelting treatment. In the report by Liu and Guo [13], both microstructure and mechanical properties of the magnesium alloy fabricated by selective laser melting were dependent on the heat treatment conditions, such as the temperature and heat treatment duration.

In order to increase the wear and corrosion resistances of magnesium alloy, surface treatments such laser surface cladding [14–16], chemical plating [17], electroplating [18], and anodic oxidation are some effective methods [19,20], among which the laser surface cladding technique has garnered a significant amount of interest recently [21–23]. For example, a coating with TiC reinforce successfully enhanced the microhardness and wear resistance by about 5–6 and 4.5–5.8 times [16]. By applying Al-Si powders to three distinct magnesium alloys (AZ61, WE54 and ZK30) with a laser of Nd:YAG, Bernabe et al. [2] obtained coatings with no cracks, no pores, and strong metallurgical bonding. Lei et al. [24] produced dense, crack and porous-free Al-Si coatings with a saw-tooth form and strong metallurgical bonding on the surface of AZ91D magnesium alloy. Al +  $Al_2O_3$  powders were laser-cladded onto a magnesium alloy surface by Hazra et al. [25], which resulted in decreased wear rate relative to the magnesium alloy substrate.

Laser cladding experiments on magnesium alloy surfaces to improve their properties have a mature technical foundation, and the addition of rare earth oxides plays an invaluable role in the modification of original powders in laser cladding. Zhu et al. [26] studied the impact of the addition of  $Y_2O_3$  on the surface of magnesium alloy on Al-Cu cladding coating. Their findings demonstrated that  $Y_2O_3$  considerably improved the mechanical characteristics and gave rise to a microstructure that was dendritic, striped, or dispersed granular. Yang and co-authors [27] prepared Al-TiC-Al<sub>3</sub>Ti composites containing  $Y_2O_3$  (0–2 wt.%) on AZ91D matrix by laser cladding. When an appropriate amount of  $Y_2O_3$  was introduced into the coating, it is found that the TiC phase within the composite coating is fine and dispersed. The addition of  $Y_2O_3$  enhances the mechanical properties and corrosion resistance of the cladding. By using laser surface cladding, Bu et al. [28] successfully created Al-TiC- $Y_2O_3$  composite coating on the surface of AZ63-Er alloy. The results showed that the hardness of the cladding layer containing  $Y_2O_3$  is higher than that without adding  $Y_2O_3$ , and has the highest corrosion resistance as it contains 0.6%  $Y_2O_3$ . At present, there are very few studies on yttrium oxide modification of Al-Si coating. In this study, therefore, the effect of adding different amount of  $Y_2O_3$  from 1 to 2 wt.% on the microstructure as well as properties of Al-Si laser clad layer above AZ91D magnesium alloy surface has been analyzed. The properties of the coatings were systematically evaluated in terms of the microhardness measurement, wear and corrosion testing experiments.

## 2. Materials and Methods

### 2.1. Sample Preparation

The AZ91D magnesium alloy employed as the matrix material for this study has a geometry of  $100 \times 50 \times 15 \text{ mm}^3$ . Table 1 displays the AZ91D chemical composition. The primary coating powder is Al-12Si (wt.%, the same as following). The Al-12Si powder has a size in the range from 100 to 150  $\mu\text{m}$ . The rare earth oxide  $Y_2O_3$  (99.99% purity and 75  $\mu\text{m}$  mean powder size) with 1.0, 1.5 and 2.0 wt.%, respectively, has been incorporated into the primary powders to investigate how it affects the coatings microstructure and properties. Four groups of cladding powders, illustrated in Table 2, were created.

**Table 1.** Chemical composition (wt.%) of AZ91 magnesium alloy.

Al	Zn	Mn	Si	Fe	Cu	Ni	Be	Mg
9.3	0.63	0.32	0.05	0.003	0.021	0.001	0.001	Bal.

**Table 2.** Samples and composition (wt.%) of coatings.

Title 1	Title 2
AS	Al-12Si
AS1Y	Al-12Si + 1 $Y_2O_3$
AS1.5Y	Al-12Si + 1.5 $Y_2O_3$
AS2Y	Al-12Si + 2 $Y_2O_3$

Before laser cladding, use 60 to 1500 mesh metallographic sandpaper to grind the surface of the substrate, wash away the abrasive debris with deionized water and dry it. The surface was then roughened by sandblasting with  $Al_2O_3$ , and finally ultrasonically cleaned with acetone, alcohol and deionized water in sequence. At least three specimens per group were made in order to evaluate performance and study microstructure and to acquire accurate data.

### 2.2. Laser Cladding Process

For the cladding treatment, a YAG fiber laser having the maximum power of 6 kW was employed. Laser cladding used synchronous powder feeding. Studies have shown that high output power is conducive to the formation of a more uniform microstructure,

but too high power or too low scanning speed will lead to surface evaporation and pit formation, while too low power or too high scanning speed will lead to insufficient melting, inhomogeneous particle distribution and failure of the bonding interface. Following several experiments, the following technical settings were determined to be optimal: 1 kW laser power, 6 mm/s scanning velocity, 3 mm laser beam size, and 1.2 r/min powder feeding rate. Meanwhile, high-purity argon was employed as the shielding gas due to the easy oxidation of the laser cladding procedure. Figure 1 shows a schematic illustration of the laser cladding process.

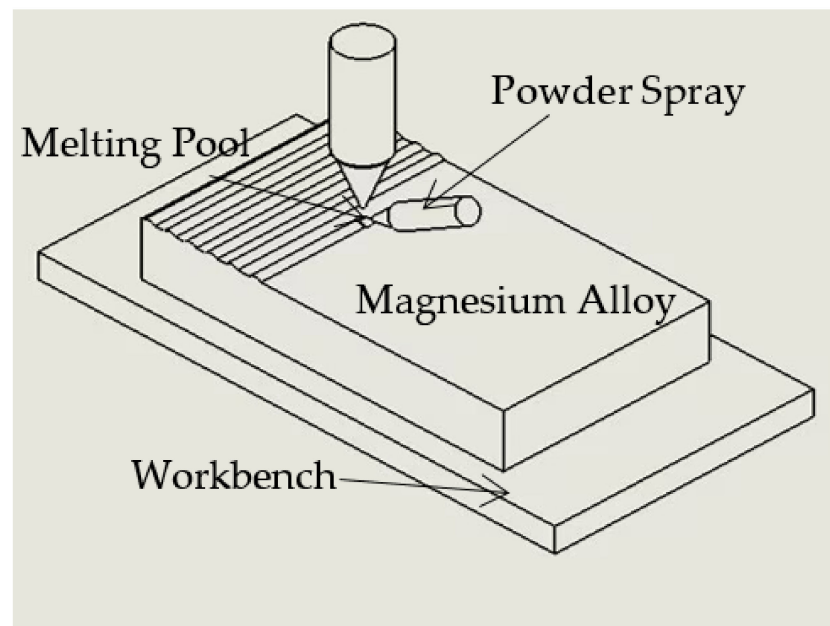


**Figure 1.** Schematic illustration of the laser cladding process.

### 2.3. Microstructure and Phase Analysis

The specimens were machined into size of  $10 \times 10 \times 5 \text{ mm}^3$  by wire cutting for testing. From the cross-section of the laser-clad samples, microstructural investigations were performed using a GeminiSEM 300 scanning electron microscope (SEM). Phase constituents were analyzed using an Ultima IV multipurpose X-ray diffractometer (XRD), with the scanning  $2\theta$  in a range from  $10$  to  $90^\circ$ . Surface morphologies of the as-cladded coatings, as well as the coatings after wear test and corrosion test, were characterized by optical microscope (OM) and SEM, respectively.

### 2.4. Investigation of the Mechanical, Wear and Corrosion Properties

A TMVS-1 Vickers microhardness tester was used to measure the microhardness, with a force of 100 gf (0.98 N) and hold for 10 s during measurement. Each microhardness point was determined by performing five consecutive measurements on the coated cross section at the same depth and averaging the results. The sliding tribological test was performed in dry condition using an MPX-3G pin-disk friction wear tester. The grinding process lasted 15 min with a 50 N experimental load. The wear volume and worn surface morphologies have been analyzed following the previous studies [29,30]. Use epoxy resin to encapsulate the sample to be tested, and use CHI660e electrochemical workstation to test the Tafel polarization curve. The working electrode was the sample, the auxiliary electrode was a platinum sheet, and the reference electrode was a saturated calomel electrode. The electrolyte employed was a 3.5% NaCl solution.

### 3. Results and Discussion

#### 3.1. Microstructural Study

The XRD patterns of the laser-clad Al-12Si coating and the  $Y_2O_3$ -modified coatings are shown in Figure 2. It can be seen that  $\alpha$ -Mg and  $Mg_2Si$  phases have formed in the unmodified coating, and the diffraction peak intensities of these two phases are relatively high. Moreover, they are also accompanied by the production of a certain amount of  $Al_{12}Mg_{17}$  and  $Al_3Mg_2$  phases. In addition to  $Mg_2Si$  and  $Al_{12}Mg_{17}$  phases,  $Al_4MgY$  is newly formed phase in the  $Y_2O_3$  modified coating. Furthermore, no other contamination phases were observed within the coatings, which might be because rare earth elements have a purifying impact on the molten pool during process.

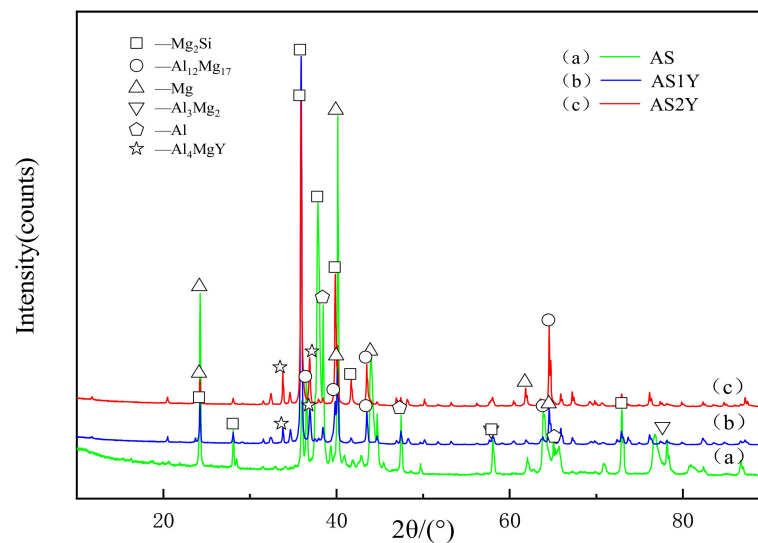


**Figure 2.** XRD patterns of the laser clad coatings on AZ91D substrate: (a), (b) and (c).

Figure 3 displays the optical micrographs of the Al-Si powder coated samples with and without  $Y_2O_3$ . By comparing the morphologies of these four samples, it can be clearly observed that the eutectic structure and particle phase of the coating without adding rare earth oxides are coarse and massive, and the distribution of the microstructure is relatively concentrated. After adding  $Y_2O_3$ , the thick eutectic structure and massive phase structure become small and distributed uniformly, and the dendritic structure is significantly refined. The results show that rare earth has an obvious effect on the microstructure refinement of the laser clad layer.

Figure 4 displays the cross-sectional morphology of the coating as seen by scanning electron microscopy. From the figure, it can be seen that the coating is divided into the cladding layer, the bonding zone and substrate. The results show that there is a strong metallurgical connection at the contact between the molten cladding layer and the substrate. There are no noticeable pores or flaws in any of the cladding layers. From each cladding layer area, the dendrite structure obviously shows a tendency to grow towards the top of the cladding layer. The cladding layer has a large number of dendrites and part of the cellular structure as shown in Figure 4a. Figure 4b,c show that there are clear columnar dendrites close to the substrate at the bottom of the cladding layer, which should be due to the large heat dissipation rate at the substrate. The temperature gradient becomes smaller, and the nucleus-forming rate is improved, thus resulting in the grain growth in a very short time with relatively strong directionality [31]. Furthermore, the cladding layer microstructure changes from coarse directed dendrites to fine equiaxed dendrites. The cladding layer structures are changed due to the addition of  $Y_2O_3$ , which acts as the nucleation center of dendrites [8], preventing dendrite coarsening and decreasing the dendrite arm spacing underneath the molten pool's non-equilibrium solidification and the influence of convective disturbance. As shown in Figure 4b, some dendritic and rod-like

structures are distributed within the cladding coating layer, and the dendrite distribution is aggregated. Figure 4c shows that the rod-like structure in the cladding layer becomes short and thick with a little petal-like structure, and the structure distribution is more uniform. Figure 4d displays the AS2Y cladding layer. The directionality of the dendritic structure in the coating is no longer obvious from Figure 4d, and the eutectic structure tends to be more refined. The microstructure of the Al-Si + Y<sub>2</sub>O<sub>3</sub> coating exhibits a dendritic eutectic structure with varying degrees of refinement in comparison to the coating without Y<sub>2</sub>O<sub>3</sub>, and the dendritic eutectic tends to distribute uniformly, which would be beneficial to a high microhardness, low wear rate and great corrosion performance of the coatings [26].

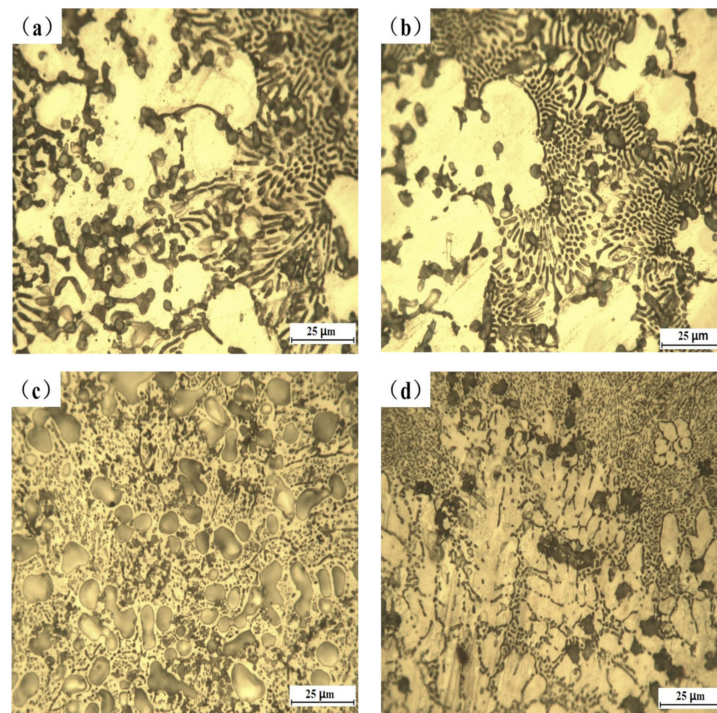


**Figure 3.** Optical micromorphology of cladded samples: (a) AS, (b) AS1Y, (c) AS1.5Y, and (d) AS2Y.

As shown in Figure 4e, three typical microstructural areas of A, B, and C are selected on the surface of the AS coating for SEM-EDS chemical composition analysis. Among them, zones A and B are blocky and strip-shaped with lighter color, respectively. The microstructures measured in area C are small particles with darker color. Based on the test results in Table 3, it is found that the structure measured in the strip region B is rich in Mg and Al elements, with an atomic ratio of nearly 1.4:1, so it can be inferred that the intermediate phase in the region is mainly Al<sub>12</sub>Mg<sub>17</sub>. It can be seen from the measurement results of C that the main elements in this area are Mg and Si. Combined with XRD analysis, it can be concluded that the substances in this area are mainly Mg<sub>2</sub>Si. The high magnification SEM image of AS2Y coating presents that the microstructure morphologies are fine stripes, and the structures are more dense and uniform, which have been shown in Figure 4f. Combined with the SEM-EDS measurement results in Table 3, it can be seen that most of the Y<sub>2</sub>O<sub>3</sub> particles have dissolved and decomposed into Y due to the strong metallurgical reaction. The Y atoms in the cladding coating are primarily distributed at the grain boundaries due to the greater atomic radius of Y of 0.18 nm [32]. Rare earth element Y acts as a non-homogeneous nucleus to inhibit grain growth by dragging effect on grain boundaries, thus inhibiting the growth of dendritic grains [33]. In addition, the high melting point of Y<sub>2</sub>O<sub>3</sub>, because of the increased content, it requires more energy to disintegrate and reduces the molten pool lifespan, thus the crystal does not have enough time to grow [16].

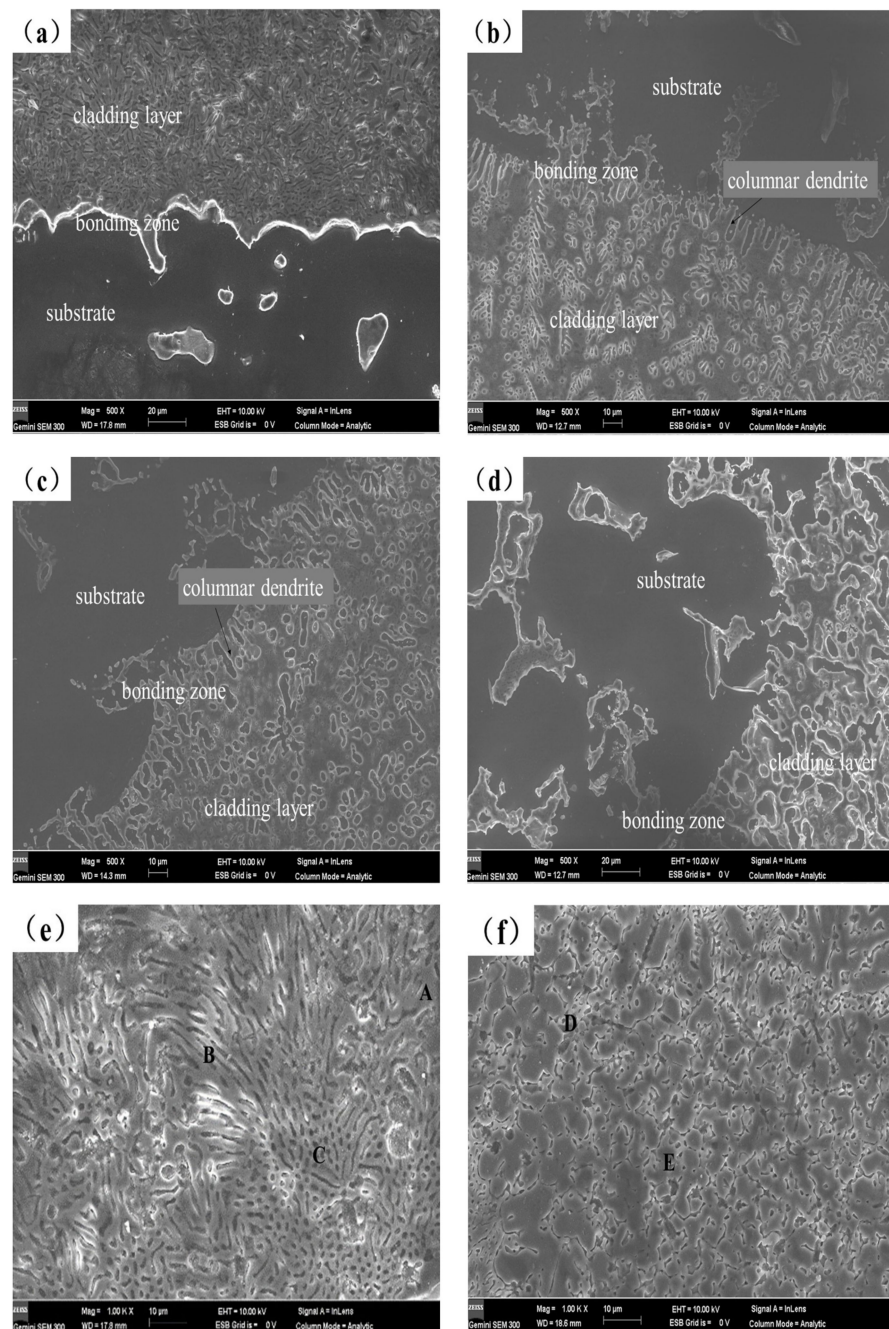


**Figure 4.** SEM microstructures of laser cladded coatings in this study: (a) AS, (b) AS1Y, (c) AS1.5Y, (d) AS2Y, (e) AS under magnification (Positions A, B and C are the EDS analysis area), and (f) AS2Y under magnification (Positions D and E are the EDS analysis area).

**Table 3.** Chemical compositions of the microstructure analyzed by SEM-EDS (wt.%).

Position	Al	Mg	Si	Y	O
A	41.0	58.1	0.9	0	0
B	42.1	51.3	6.6	0	0
C	14.7	45.8	39.6	0	0
D	74.7	3.6	19.6	2.0	0.1
E	65.6	4.6	28.7	1.2	0

### 3.2. Microhardness Analysis

Figure 5 shows the microhardness measurement results and indentation morphologies of the laser clad sample sections. The curves in Figure 5 show that all the clad samples have a similar tendency in terms of the microhardness distribution over the coating depth, which is consistent with the variation of the indentation dimension. The test results show that the test indentation steadily increases from the upper surface of the cladding to the substrate, indicating that the cladding surface has the highest hardness. Measurements of the hardness of coatings containing  $Y_2O_3$  in comparison to the AS cladding layer show a significant improvement. The microhardness of all clad coatings is higher than that of the substrate, which is about 75 HV, and the average microhardness of the cladding layer of AS2Y coating reaches the highest (about 270 HV), and the average microhardness of the AS cladding layer is only 220 HV. The addition of  $Y_2O_3$  can refine the grain and introduce more grain boundaries. The grain boundary reinforcement and dislocation strengthening are conducive to the improvement in the coating microhardness. Additionally, the production of intermetallic compounds  $Mg_2Si$  and  $Al_4MgY$  has a favorable impact on enhancing the hardness of the laser-clad layer, as evidenced by the examination of microstructure, XRD, and SEM-EDS data [4].

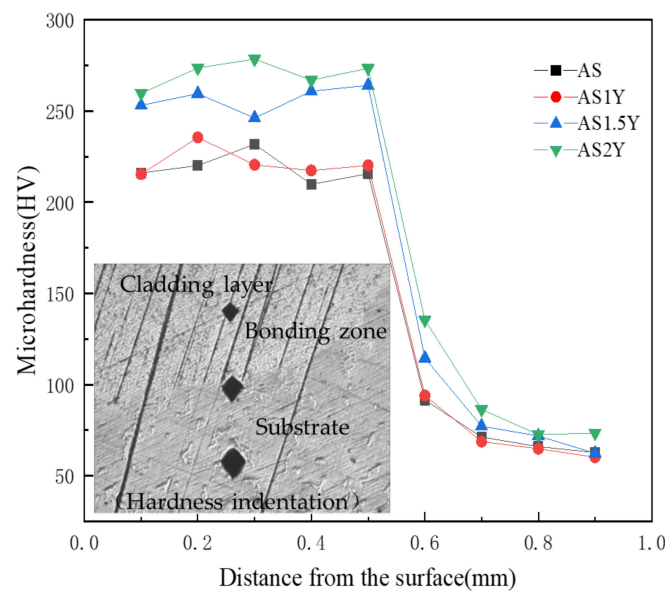
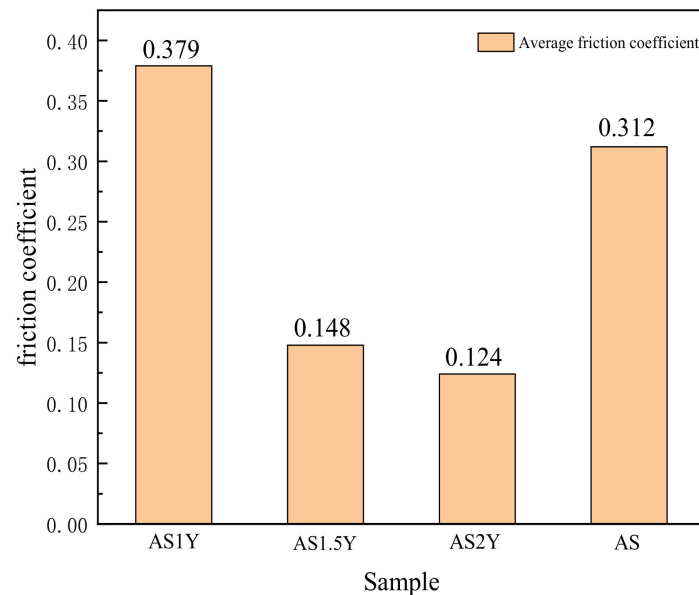


**Figure 5.** Microhardness distribution across the cross-section of coatings.

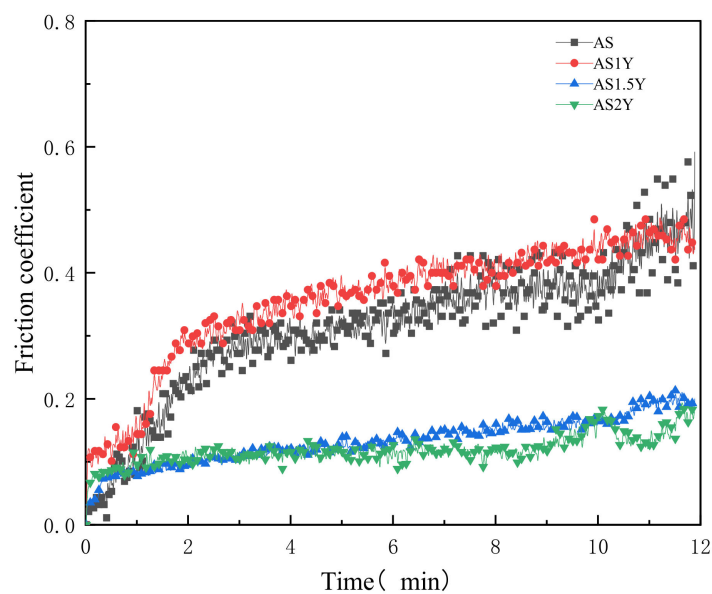
### 3.3. Wear Analysis

A key indicator of abrasion resistance is the friction coefficient. Figure 6a shows the average friction coefficient of various coatings investigated in the current study. The average friction coefficient of the coating shows a lower trend with increasing  $Y_2O_3$  content, which may indicate a steady increase in the wear resistance of the coating. The transient friction coefficients versus time are shown in Figure 6b. As can be seen from the figure, the friction coefficient rises rapidly with increasing friction time, and then tends to stabilize. The rise in abrasive dust at the surface, which alters the dimension of the practical contact area and the localized contact load, may be the cause of the rapid increase in friction coefficient [34]. Because floating slag and gas can inevitably generate impurities and pores in the surface layer, AS1Y coating's average friction coefficient is a little bit higher than coatings without  $Y_2O_3$  addition. However, the overall dynamic friction coefficient variation is smoother for the AS1Y coatings compared to the coatings without  $Y_2O_3$ . Rare earth Y elements could present wetting effect within the microstructure on account of its surface activity and mobility in the molten pool, which makes the microstructure distribution more uniform. According to the results, the friction coefficient of AS2Y coating displays the lowest value, which is about 60% lower than that of AS coating, and the fluctuation is the most stable,

showing good wear resistance. It is worth to note that the friction coefficients obtained in this study in Figure 6 are much lower than the generally reported dry sliding friction coefficient in a range of about 0.5–0.8 for most of metallic materials [35–38]. According to the results displayed in Figure 6, it has been found that addition of  $Y_2O_3$  acts as a solid lubricant during dry sliding and is effective into reducing the friction coefficient. The friction coefficient of the iron-based alloy coating prepared by Wang et al. [39] was reduced by about 0.1 due to the addition of  $La_2O_3$ . He et al. [40] fabricated Al-TiC-CeO<sub>2</sub> coatings with a minimum friction coefficient of about 0.5. The friction coefficient of the ASY coatings prepared in this work is significantly reduced.



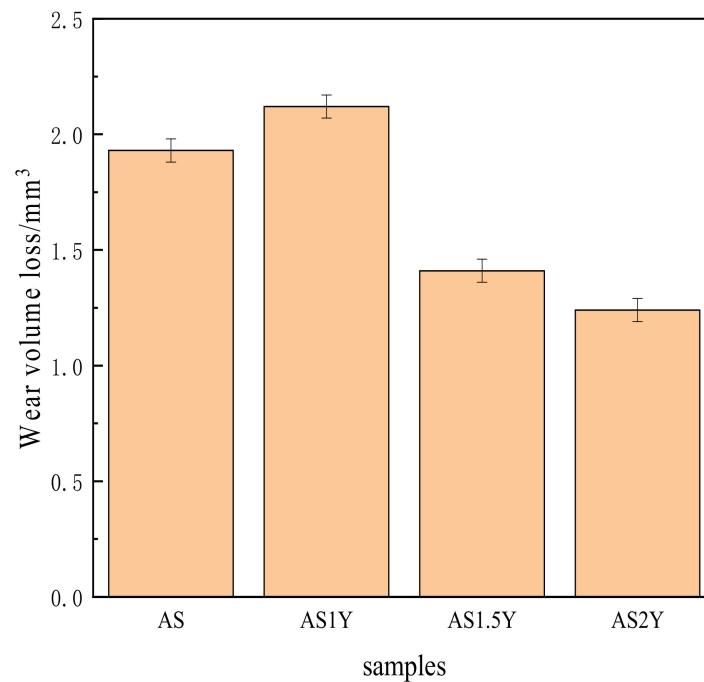
(a)



(b)

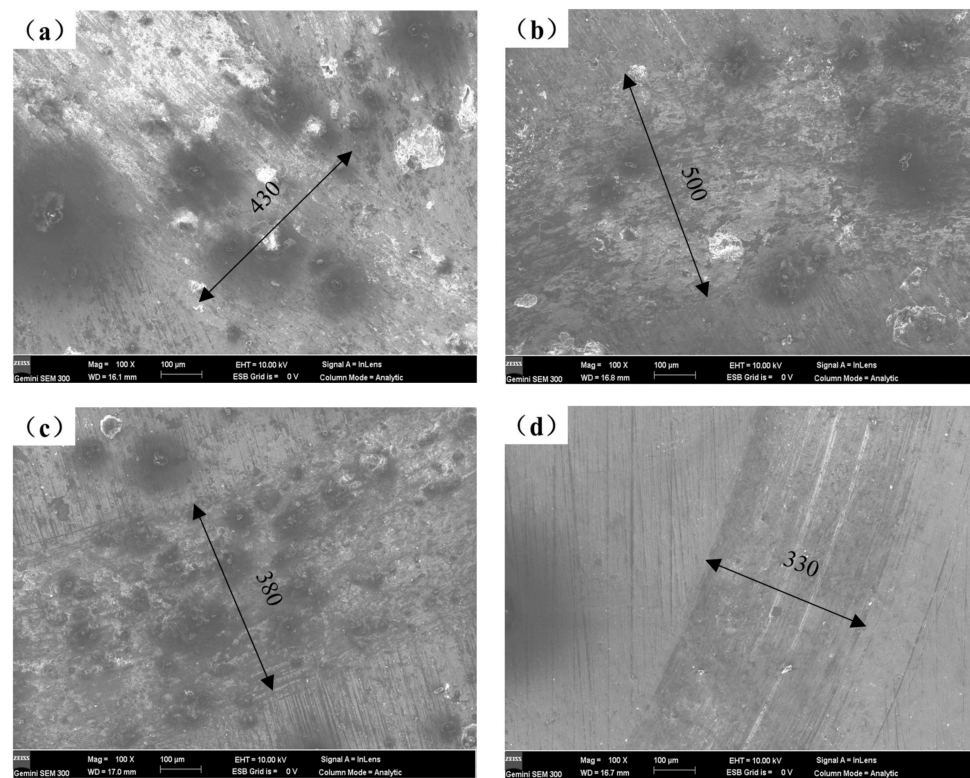
**Figure 6.** Comparison of the friction coefficient between the unmodified and  $Y_2O_3$ -modified coatings: (a) average friction coefficient, and (b) friction coefficient evolution history.

Figure 7 shows the wear volume loss of the cladding layer after 15 min of anti-grinding. The figure clearly shows that the AS2Y cladding layer's wear volume loss is substantially smaller than that of the AS coating, demonstrating that the addition of  $Y_2O_3$  can somewhat reduce the coating's wear loss and increase its wear resistance. In fact, the evolution tendency of the wear volume loss in Figure 7 is consistent with the microhardness results in Figure 5. According to Deng et al. [29,30,38], a higher wear resistance or lower wear volume loss is generally obtained by increasing the mechanical strength and microhardness of a metallic material.



**Figure 7.** Influence of  $Y_2O_3$  addition on the wear volume losses of the coatings.

The worn surface morphologies of various coatings as seen under SEM are displayed in Figure 8. Comparing the wear scars of the four samples, it is observed that under the same magnification, the width of the wear scars gradually decreases with the increase of  $Y_2O_3$  content. The wear scar width of the coating falls from approximately 500 to 330  $\mu m$ , as illustrated in Figure 8b–d, as the  $Y_2O_3$  content rises from 1 to 2 wt%. The wear mechanism of the coatings investigated is a combination of abrasive and adhesive wear [2], and the adhesive zones are clearly visible. As seen in Figure 8b–d, the degree of wear of coatings containing  $Y_2O_3$  gradually declines, with minor wear and micro-cuts serving as the primary wear features. The improvement in wear resistance is due to the formation of a refined  $Mg_2Si$  phase in the microstructure, which acts as a pressure-bearing agent on the friction surface. Meanwhile, the addition of  $Y_2O_3$  may improve the microstructure of the coating and make the hard phase dispersed distribution, thus improving the uniformity of the microstructure. As mentioned above, the microstructure of the coating is altered by the addition of  $Y_2O_3$ , going from columnar dendrites to a fine-grained cellular network structure, greatly increasing the hardness of the composite coating. Therefore, it is more difficult for the friction pair to press into the coating surface, and the wear resistance of the coating can be significantly improved. In addition,  $Y_2O_3$  may hasten the convection of the molten pool and encourage a uniform distribution of the hard phase, which may in part contribute to the wear resistance of the cladding layer due to the reinforcement of the dispersion.



**Figure 8.** Worn surface morphologies of different coatings: (a) AS, (b) AS1Y, (c) AS1.5Y, and (d) AS2Y.

### 3.4. Corrosion Resistance Analysis

Figure 9 depicts the potentiodynamic polarization curves of the test specimens in a 3.5 weight percent solution of NaCl at room temperature, and Table 4 lists the electrochemical parameters that were obtained from Figure 9. Lower corrosion current values correspond to lower corrosion rates and greater corrosion resistance of the coating in terms of corrosion dynamics [33]. The data in Table 4 shows that the corrosion resistance of the coating created by laser cladding on the AZ91D magnesium alloy substrate is greatly improved compared to the uncoated AZ91D, and with the content of  $Y_2O_3$  increasing the corrosion current density of the coating generally increases first and then decreases. When the  $Y_2O_3$  content in the coating reaches 2%, the corrosion potential of AS2Y sample is the highest ( $-1.284$  V), and the corrosion current density reaches the lowest ( $7.027 \times 10^{-5}$  A/cm<sup>2</sup>) among all the samples tested, which indicates the best corrosion resistance. Figure 10 shows the surface corrosion morphologies of AZ91D, AS and AS2Y samples after salt-immersion tests in 3.5 wt.% NaCl solution for 72 h. It can be observed that the corrosion surface of AZ91D in Figure 10a tends to develop vertically accompanied by deep and large corroded pores, which indicates the poor corrosion resistance. In the case of AS sample in Figure 10b, the occurrence of homogeneously uniform features with few pitting corrosion sites is evidenced at the specimen surface. Figure 10c shows no obvious pitting, with some micro-cracking on the surface. Figure 10d corrosion surface smooth without cracks produced, a very small part of the surface shows micro-pitting. In contrast, the surface of AS2Y sample in Figure 10e presents quite flat characteristics without pitting corrosion sites, indicating a superior corrosion resistance. Thus, adding  $Y_2O_3$  to coatings is a viable technique to improve the corrosion behavior of AZ91D magnesium alloy, much like adding calcium to AZ31 magnesium alloy [41].

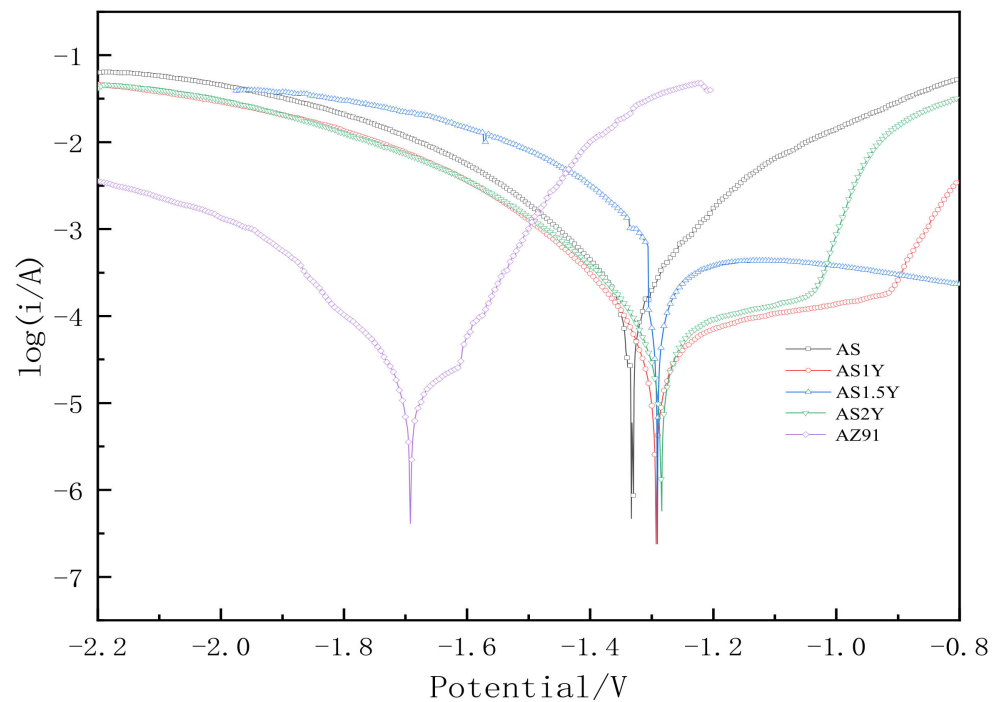
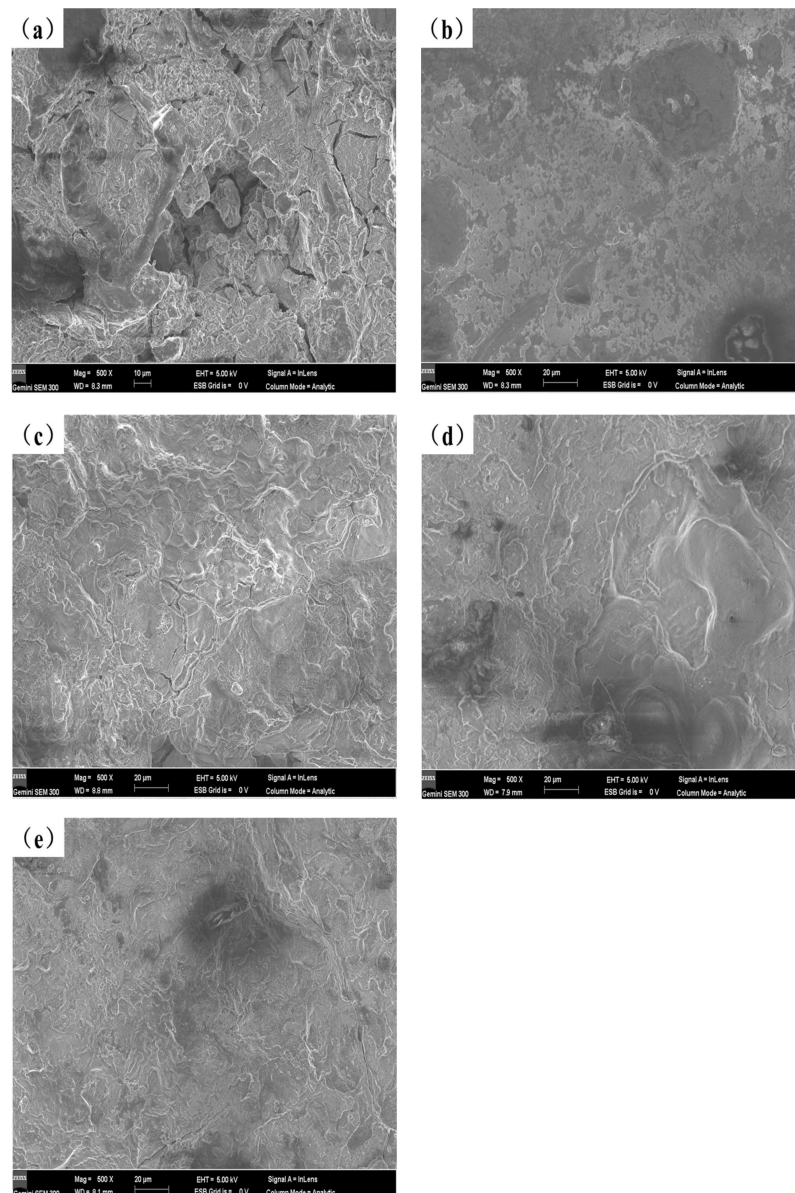


Figure 9. Potentiodynamic polarization curve.

Table 4. Electrochemical parameters calculated from the results in Figure 9.

Sample	$E_{corr}/V$	$I_{corr}/(A \cdot cm^{-2})$	$\beta_a/V$	$\beta_c/V$	$R_p/\Omega$
AZ91D	-1.692	$1.22 \times 10^{-3}$	0.376	-0.164	40.696
AS	-1.333	$7.466 \times 10^{-5}$	0.127	-0.143	391.706
AS1Y	-1.293	$9.85 \times 10^{-5}$	0.330	-0.122	393.162
AS1.5Y	-1.287	$8.737 \times 10^{-5}$	0.296	-0.151	497.988
AS2Y	-1.284	$7.027 \times 10^{-5}$	0.391	-0.129	600.158

The results show that the improved corrosion resistance of the  $Y_2O_3$ -modified coatings is mostly the result of structural changes within the coatings, suggesting that the corrosion of the  $Y_2O_3$ -modified specimens is in the passivation phase [26]. Shao et al. [42] recently reported the link between the microstructure and corrosion behavior of the magnesium alloy AZ91D. The introduction of rare earth elements into coatings has the effect of purifying the melt, purifying grain boundaries and inhibiting the growth of crystal columns for the molten pool metal in the laser cladding process [43], which has also been observed in the cross-sectional morphologies of the coatings mentioned above. As the  $Y_2O_3$  content increases, the content of non-metallic inclusions and impurities in the coating structure are significantly reduced, and the metallurgical structure of the coating tends to denser, especially the existence of porosity and inhomogeneity would be reduced. Similar phenomenon has also been found by Qi et al. [44]. Meanwhile, the coarse dendrites, reticulated eutectic structures and bulk grains in the Al-Si +  $Y_2O_3$  cladding layer tend to be refined. Thus, in general, refined grain size conduces to suppression of corrosion rate. In addition, the dispersion distribution of compound phases such as  $Mg_2Si$  and  $Al_4MgY$  plays a positive influence in improving the average corrosion potential and delaying the galvanic corrosion of the cladding layer, and the formation of these phases greatly reduces the amount of  $\alpha$ -Mg used as the anode, which reduces the occurrence of intergranular corrosion, thereby lowering the rate of corrosion and increasing the corrosion resistance of samples.



**Figure 10.** Surface morphology of different coatings after corrosion test in 3.5 wt.% NaCl solution: (a) AZ91D, (b) AS, (c) AS1Y, (d) AS1.5Y, (e) AS2Y.

#### 4. Conclusions

By using laser cladding technology, Al-Si +  $Y_2O_3$  coatings were created on the surface of AZ91D magnesium alloys, and the impact of  $Y_2O_3$  content on the microstructure and characteristics of the Al-Si coatings was investigated. The outcomes of the trial revealed that:

- (1) The microstructures of Al-Si +  $Y_2O_3$  cladding layer include  $\alpha$ -Mg,  $Mg_2Si$ ,  $Al_4MgY$  phases and a small amount of  $Al_{12}Mg_{17}$  phase. With the increase of the amount of  $Y_2O_3$  added, the coarse dendrites, reticulated eutectic structures and massive phases in the Al-Si +  $Y_2O_3$  cladding layer tend to be refined and gradually uniform distribution.
- (2) With an increase in  $Y_2O_3$  content, the microhardness of the Al-Si coating increases. When the content of  $Y_2O_3$  reaches about 2 wt.%, the microhardness of the coating reaches the greatest with an value of about 270 HV.
- (3) Friction experiments show that increasing the  $Y_2O_3$  content, the average friction coefficient and the wear scar width of the coating have decreased. In addition, the

Y<sub>2</sub>O<sub>3</sub> addition promotes the reduction of wear volume loss of the cladding layer, which effectively decreases the wear rate of the magnesium substrate.

- (4) The Y<sub>2</sub>O<sub>3</sub>-modified coatings have greater corrosion resistance than the untreated coatings. The addition of Y<sub>2</sub>O<sub>3</sub> promotes the reduction of localized corrosion sites and makes the corrosion surface smoother, implying that the corrosion resistance increases significantly.

**Author Contributions:** Conceptualization, X.W.; methodology, X.W., C.T. and Y.L.; validation, C.T., Y.L. and S.Q.; formal analysis, C.T. and Y.L.; investigation, X.W., C.T., L.S. and L.W.; data curation, C.T. and J.Z.; writing—original draft preparation, C.T.; writing—review and editing, X.W., L.S. and L.W.; supervision, L.S. and L.W. All authors have read and agreed to the published version of the manuscript.

**Funding:** Technological Production Translation of Jiangsu Province (BA2015129); and Australian Research Council (DE180100124).

**Institutional Review Board Statement:** Not applicable.

**Informed Consent Statement:** Not applicable.

**Data Availability Statement:** Not applicable.

**Acknowledgments:** The authors are grateful to the support of Jiangsu Overseas Visiting Scholar Program for University Prominent Young & Middle-aged Teachers and Presidents (2017), the “Qinglan” Project Foundation of Jiangsu Province (2016), and the Technological Production Translation of Jiangsu Province (BA2015129). The authors thank Nantong University Analysis & Testing Center for the technical support. The author L.S. would like to acknowledge the support from Australian Research Council (ARC) through Discovery Early Career Researcher Award (DECRA) fellowship.

**Conflicts of Interest:** The authors declare no conflict of interest.

## References

- Jiang, J.H.; Zhou, Q.; Yu, J.S.; Ma, A.B.; Song, D.; Lu, F.M.; Zhang, L.Y.; Yang, D.H.; Chen, J.Q. Comparative analysis for corrosion resistance of micro-arc oxidation coatings on coarse-grained and ultra-fine grained AZ91D Mg alloy. *Surf. Coat. Technol.* **2013**, *216*, 259–266. [[CrossRef](#)]
- Carcel, B.; Sampedro, J.; Ruescas, A.; Toneu, X. Corrosion and wear resistance improvement of magnesium alloys by laser cladding with Al-Si. *Phys. Procedia* **2011**, *12*, 353–363. [[CrossRef](#)]
- Liu, F.J.; Ji, Y.; Meng, Q.S.; Li, Z.S. Microstructure and corrosion resistance of laser cladding and friction stir processing hybrid modification Al-Si coatings on AZ31B. *Vacuum* **2016**, *133*, 31–37. [[CrossRef](#)]
- Yang, Y.; Wu, H. Improving the wear resistance of AZ91D magnesium alloys by laser cladding with Al-Si powders. *Mater. Lett.* **2009**, *63*, 19–21. [[CrossRef](#)]
- Cao, X.; Jahazi, M.; Immarigeon, J.P.; Wallace, W. A review of laser welding techniques for magnesium alloys. *J. Mater. Process. Technol.* **2006**, *171*, 188–204. [[CrossRef](#)]
- Asghar, O.; Li-Yan, L.; Yasir, M.; Chang-Jiu, L.; Cheng-Xin, L. Enhanced Tribological Properties of LA43M Magnesium Alloy by Ni60 Coating via Ultra-High-Speed Laser Cladding. *Coatings* **2020**, *10*, 638. [[CrossRef](#)]
- Zhang, X.L.; Zhang, K.M.; Zou, J.X. Microstructures and properties in surface layers of Mg-6Zn-1Ca magnesium alloy laser-clad with Al-Si powders. *Trans. Nonferrous Met. Soc. China* **2018**, *28*, 96–102. [[CrossRef](#)]
- Liu, J.L.; Yu, H.J.; Chen, C.Z.; Weng, F.; Dai, J.J. Research and development status of laser cladding on magnesium alloys: A review. *Opt. Lasers Eng.* **2017**, *93*, 195–210. [[CrossRef](#)]
- Mo, N.; Tan, Q.Y.; Bermingham, M.; Huang, Y.D.; Dieringa, H.; Hort, N.; Zhang, M.X. Current development of creep-resistant magnesium cast alloys: A review. *Mater. Des.* **2018**, *155*, 422–442. [[CrossRef](#)]
- Abbas, G.; Li, L.; Ghazanfar, U.; Liu, Z. Effect of high power diode laser surface melting on wear resistance of magnesium alloys. *Wear* **2006**, *260*, 175–180. [[CrossRef](#)]
- Ren, Z.; Zhao, Y.; Han, G.; Wang, W.; Zhou, K.; He, T.; Sun, Y. Laser-Arc Hybrid Cladding of Al-Mg Alloy Coating on AZ80 Mg Alloy: Effect of Laser Beam Oscillations Amplitude. *Materials* **2022**, *15*, 7272. [[CrossRef](#)] [[PubMed](#)]
- Riquelme, A.; Rodrigo, P. An Introduction on the Laser Cladding Coatings on Magnesium Alloys. *Metals* **2021**, *11*, 1993. [[CrossRef](#)]
- Liu, S.; Guo, H. Influence of Heat Treatment on Microstructure and Mechanical Properties of AZ61 Magnesium Alloy Prepared by Selective Laser Melting (SLM). *Materials* **2022**, *15*, 7067. [[CrossRef](#)] [[PubMed](#)]
- Taltavull, C.; Torres, B.; López, A.J.; Rodrigo, P.; Rams, J. Novel laser surface treatments on AZ91 magnesium alloy. *Surf. Coat. Technol.* **2013**, *222*, 118–127. [[CrossRef](#)]

15. Wang, A.H.; Yue, T.M. YAG laser cladding of an Al-Si alloy onto an Mg/SiC composite for the improvement of corrosion resistance. *Compos. Sci. Technol.* **2001**, *61*, 1549–1554. [[CrossRef](#)]
16. Zhang, H.X.; Dai, J.J.; Ma, Z.W.; Wang, X.Y.; Zhang, N.L. Effect of  $Y_2O_3$  on microstructures and wear resistance of TiC reinforced Ti-Al-Si coating by laser cladding on TC4 alloy. *Surf. Rev. Lett.* **2019**, *26*, 1950077. [[CrossRef](#)]
17. Thakur, A.; Gharde, S.; Kandasubramanian, B. Electroless nickel fabrication on surface modified magnesium substrates. *Def. Technol.* **2019**, *15*, 636–644. [[CrossRef](#)]
18. Kang, Z.X.; Li, W. Facile and fast fabrication of superhydrophobic surface on magnesium alloy by one-step electrodeposition method. *J. Ind. Eng. Chem.* **2017**, *50*, 50–56. [[CrossRef](#)]
19. Saranya, K.; Bhuvaneshwari, S.; Chatterjee, S.; Rajendran, N. Titanate incorporated anodized coating on magnesium alloy for corrosion protection, antibacterial responses and osteogenic enhancement. *J. Magnes. Alloy.* **2022**, *10*, 1109–1123. [[CrossRef](#)]
20. Pan, S.; Tu, X.H.; Yu, J.X.; Zhang, Y.; Miao, C.P.; Xu, Y.L.; Fu, R.; Li, J.Y. Optimization of AZ31B Magnesium Alloy Anodizing Process in NaOH-Na<sub>2</sub>SiO<sub>3</sub>-Na<sub>2</sub>B<sub>4</sub>O<sub>7</sub> Environmental-Friendly Electrolyte. *Coatings* **2022**, *12*, 578. [[CrossRef](#)]
21. Tan, C.; Zhu, H.; Kuang, T.; Shi, J.; Liu, H.; Liu, Z. Laser cladding Al-based amorphous-nanocrystalline composite coatings on AZ80 magnesium alloy under water cooling condition. *J. Alloys Compd.* **2017**, *690*, 108–115. [[CrossRef](#)]
22. Riquelme, A.; Rodrigo, P.; Escalera-Rodriguez, M.D.; Rams, J. Evaluation of the Wear Resistance and Corrosion Behavior of Laser Cladding Al/SiC Metal Matrix Composite Coatings on ZE41 Magnesium Alloy. *Coatings* **2021**, *11*, 639. [[CrossRef](#)]
23. Tokunaga, T.; Ohno, M.; Matsuura, K. Coatings on Mg alloys and their mechanical properties: A review. *J. Mater. Sci. Technol.* **2018**, *34*, 1119–1126. [[CrossRef](#)]
24. Lei, Y.W.; Sun, R.L.; Tang, Y.; Niu, W. Experimental and thermodynamic investigations into the micro-structure of laser clad Al-Si coatings on AZ91D alloys. *Surf. Coat. Technol.* **2012**, *207*, 400–405. [[CrossRef](#)]
25. Hazra, M.; Mondal, A.K.; Kumar, S.; Blawert, C.; Dahotre, N.B. Laser surface cladding of MRI 153M magnesium alloy with (Al + Al<sub>2</sub>O<sub>3</sub>). *Surf. Coat. Technol.* **2009**, *203*, 2292–2299. [[CrossRef](#)]
26. Zhu, R.D.; Li, Z.Y.; Li, X.X.; Sun, Q. Microstructure and properties of the low-power-laser clad coatings on magnesium alloy with different amount of rare earth addition. *Appl. Surf. Sci.* **2015**, *353*, 405–413. [[CrossRef](#)]
27. Yang, L.Q.; Li, Z.Y.; Zhang, Y.Q.; Wei, S.Z.; Wang, Y.J.; Kang, Y. In-situ TiC-Al<sub>3</sub>Ti reinforced Al-Mg composites with Y<sub>2</sub>O<sub>3</sub> addition formed by laser cladding on AZ91D. *Surf. Coat. Technol.* **2020**, *383*, 125249. [[CrossRef](#)]
28. Bu, R.; Jin, A.X.; Sun, Q.; Zan, W.; He, R.L. Study on laser cladding and properties of AZ63-Er alloy for automobile engine. *J. Mater. Res. Technol.* **2020**, *9*, 5154–5160. [[CrossRef](#)]
29. Deng, G.; Chong, Y.; Su, L.; Zhan, L.; Wei, P.; Zhao, X.; Zhang, L.; Tian, Y.; Zhu, H.; Tsuji, N. Mechanisms of remarkable wear reduction and evolutions of subsurface microstructure and nano-mechanical properties during dry sliding of nano-grained Ti6Al4V alloy: A comparative study. *Tribol. Int.* **2022**, *169*, 107464. [[CrossRef](#)]
30. Deng, G.; Zhao, X.; Su, L.; Wei, P.; Zhang, L.; Zhan, L.; Chong, Y.; Zhu, H.; Tsuji, N. Effect of high pressure torsion process on the microhardness, microstructure and tribological property of Ti6Al4V alloy. *J. Mater. Sci. Technol.* **2021**, *94*, 183–195. [[CrossRef](#)]
31. Wang, X.; Pan, X.D.; Niu, Q.; He, X.Q. Microstructure and properties of laser clad Al-Si coating on AZ33M magnesium alloy. *Heat Treat. Met.* **2021**, *46*, 202–206. [[CrossRef](#)]
32. Li, H.C.; Wang, D.G.; Chen, C.Z.; Weng, F. Effect of CeO<sub>2</sub> and Y<sub>2</sub>O<sub>3</sub> on microstructure, bioactivity and degradability of laser cladding CaO-SiO<sub>2</sub> coating on titanium alloy. *Colloids Surf. B Biointerfaces* **2015**, *127*, 15–21. [[CrossRef](#)] [[PubMed](#)]
33. Quazi, M.M.; Fazal, M.A.; Haseeb, A.S.M.A.; Yusof, F.; Masjuki, H.H.; Arslan, A. Effect of rare earth elements and their oxides on tribo-mechanical performance of laser claddings: A review. *J. Rare Earths* **2016**, *34*, 549–564. [[CrossRef](#)]
34. Deng, G.; Tieu, A.K.; Lan, X.; Su, L.; Wang, L.; Zhu, Q.; Zhu, H. Effects of normal load and velocity on the dry sliding tribological behaviour of CoCrFeNiMo<sub>0.2</sub> high entropy alloy. *Tribol. Int.* **2020**, *144*, 106116. [[CrossRef](#)]
35. Saffarzade, P.; Amadeh, A.A.; Agahi, N. Study of tribological and friction behavior of magnesium phosphate coating and comparison with traditional zinc phosphate coating under dry and lubricated conditions. *Tribol. Int.* **2020**, *144*, 106122. [[CrossRef](#)]
36. Ataya, S.; Seleman, M.M.E.; Latief, F.H.; Ahmed, M.M.Z.; Hajlaoui, K.; Soliman, A.M.; Alsaleh, N.A.; Habba, M.I.A. Wear characteristics of Mg alloy AZ91 reinforced with oriented short carbon fibers. *Materials* **2022**, *15*, 4841. [[CrossRef](#)]
37. Fabre, A.; Masse, J.E. Friction behavior of laser cladding magnesium alloy against AISI 52100 steel. *Tribol. Int.* **2012**, *46*, 247–253. [[CrossRef](#)]
38. Deng, G.; Tieu, A.K.; Su, L.; Wang, P.; Wang, L.; Lan, X.; Cui, S.; Zhu, H. Investigation into reciprocating dry sliding friction and wear properties of bulk CoCrFeNiMo high entropy alloys fabricated by spark plasma sintering and subsequent cold rolling processes: Role of Mo element concentration. *Wear* **2020**, *460–461*, 203440. [[CrossRef](#)]
39. Wang, Q.; Yang, J.; Niu, W.; Li, Y.; Mao, X.; Wang, Y.; Zhang, K. Effect of La<sub>2</sub>O<sub>3</sub> on microstructure and properties of Fe-based alloy coatings by laser cladding. *Optik* **2021**, *245*, 167653. [[CrossRef](#)]
40. He, X.; Kong, D.; Song, R. Microstructures and Properties of Laser Cladding Al-TiC-CeO<sub>2</sub> Composite Coatings. *Materials* **2018**, *11*, 198. [[CrossRef](#)]
41. Chaudry, U.M.; Farooq, A.; Tayyab, K.B.; Malik, A.; Kamran, M.; Kim, J.; Li, C.; Hamad, K.; Jun, T.S. Corrosion behavior of AZ31 magnesium alloy with calcium addition. *Corros. Sci.* **2022**, *199*, 110205. [[CrossRef](#)]
42. Cui, C.; Wu, M.P.; Miao, X.J.; Gong, Y.L.; Zhao, Z.S. The effect of laser energy density on the geometric characteristics, microstructure and corrosion resistance of Co-based coatings by laser cladding. *J. Mater. Res. Technol.* **2021**, *15*, 2405–2418. [[CrossRef](#)]

43. Shao, Z.; Nishimoto, M.; Muto, I.; Sugawara, Y. Real-time in situ observation of the corrosion process of die-cast AZ91D magnesium alloy in NaCl solutions under galvanostatic polarization. *Corros. Sci.* **2021**, *192*, 109834. [[CrossRef](#)]
44. Qi, J.; Ye, Z.; Gong, N.; Qu, X.; Mercier, D.; Swiatowska, J.; Skeldon, P.; Marcus, P. Formation of a trivalent chromium conversion coating on AZ91D magnesium alloy. *Corros. Sci.* **2021**, *186*, 109459. [[CrossRef](#)]

**Disclaimer/Publisher's Note:** The statements, opinions and data contained in all publications are solely those of the individual author(s) and contributor(s) and not of MDPI and/or the editor(s). MDPI and/or the editor(s) disclaim responsibility for any injury to people or property resulting from any ideas, methods, instructions or products referred to in the content.